

A MIXED MODEL APPROACH FOR ESTIMATING REGIONAL FUNCTIONAL CONNECTIVITY FROM VOXEL-LEVEL BOLD SIGNALS

BY CHAO ZHANG^{1,a}, CHAU B. TRAN^{1,b}, SOPHIE ACHARD^{2,d},
WENDY MEIRING^{1,c} AND ALEXANDER PETERSEN^{*3,e}

¹*Department of Statistics and Applied Probability, University of California, Santa Barbara, Santa Barbara, CA, USA,*
^a*czhang@pstat.ucsb.edu;* ^b*chautran@ucsb.edu;* ^c*meiring@ucsb.edu*

²*Univ. Grenoble Alpes, CNRS, Inria, Grenoble INP, LJK, F-38000, Grenoble, France,* ^d*sophie.achard@univ-grenoble-alpes.fr*

³*Department of Statistics, Brigham Young University, Provo, UT, USA,* ^e*petersen@stat.byu.edu*

Resting state brain functional connectivity quantifies the similarity between brain regions, each of which consists of voxels at which dynamic signals are acquired via neuroimaging techniques such as blood-oxygen-level-dependent signals in functional magnetic resonance imaging. Pearson correlation and similar metrics have been adopted by neuroscientists to estimate inter-regional connectivity, usually after averaging of signals within regions. However, dependencies between signals within each region and the presence of noise could contaminate such inter-regional correlation estimates. We propose a mixed-effects model with a novel covariance structure that explicitly isolates the different sources of variability in the observed BOLD signals, including correlated regional signals, local spatiotemporal variability, and measurement error. Methods for tackling the computational challenges associated with restricted maximum likelihood estimation will be discussed. Large sample properties are discussed and used for uncertainty quantification. Simulation results demonstrate that the parameters of the proposed model parameters can be accurately estimated and is superior to the Pearson correlation of averages in the presence of spatiotemporal noise. The proposed model is also applied to a real data set of BOLD signals collected from rats to construct individual brain networks.

1. Introduction. In recent years, the rapid advancement and increasing accessibility of neuroimaging techniques, such as electroencephalogram (EEG) scans and functional magnetic resonance imaging (fMRI), data sets that record dynamic brain activity are becoming widely available to scientists and medical practitioners. The rich volume of previously unattainable data sets has consequently catalyzed broad interest in modeling and estimating functional brain connectivity, which is of paramount importance in shedding light on the evolution of pathologies such as neurodegenerative diseases or consciousness disorders.

A brain can be considered as a network. Thus, it is not surprising that network-based approaches are prevalent in connectivity modeling (Van Den Heuvel and Pol, 2010; Meskaldji et al., 2011; Kaiser, 2011). The nodes and edges in a brain network represent brain regions and connections, respectively. An edge is identified by a high degree of some similarity metric for the brain activity signals, which is usually quantified empirically by the Pearson correlation (Achard et al., 2006; Zalesky, Fornito and Bullmore, 2012; Becq et al., 2020). However, challenges arise in preprocessing and conducting robust and reproducible analyses with the massive data volumes, particularly in the case of fMRI data sets. Signals collected from human brains are frequently modeled as realizations of random fields that traverse across both

*Correspondence to: Alexander Petersen, Department of Statistics, Brigham Young University, Provo, Utah, 84602, USA

Keywords and phrases: functional brain connectivity, mixed-effects model, spatiotemporal modeling, correlation networks.

the spatial and temporal domains (Achard et al., 2011; Achard and Gannaz, 2019). These signals are usually of noisy nature due to the inherent properties of brain activity and the errors incurred by the measuring instrument (Chaimow et al., 2018; Lohmann et al., 2018; Park and Fiecas, 2022). In addition, the spatial dimension is usually high compared to the temporal dimension, thus posing difficulties in conducting efficient and reproducible analyses.

Various methods have been proposed to overcome these challenges. Achard et al. (2006) applied a wavelet transformation to obtain brain networks based on frequency-dependent correlations between regional fMRI time series. Machine learning techniques, in particular, feature embedding and clustering are investigated to classify and characterize changes in brain dynamics due to pathology or cognitive state changes (Richiardi et al., 2013). Termenon et al. (2016) studied the relationship between the reproducibility of brain networks and the subject count and fMRI scan length using the large test-retest (TRT) resting-state fMRI data set from the Human Connectome Project (HCP). In addition, Petersen et al. (2016) proposed to view the path lengths of brain networks as functions of network density; functional principal component analysis (fPCA) is then applied and covariates are regressed on functional principal component scores to study the association between connectivity and subjects' age, episodic memory, and executive function. It should be emphasized that, while some of these existing methods can localize connectivity to the subject level (Petersen et al., 2016; Bowman, 2007), the analysis phase usually requires group level information.

Functional connectivity quantification and estimation is a primary goal of these neuroscience inquiries. Following the characterization of Van Den Heuvel and Pol (2010), functional connectivity is the dependency of simultaneous neuronal activation patterns of anatomically separated brain regions. Consequently, rather than directly modeling signals at the voxel level, the vast majority of existing studies aggregate signals within certain and use an intuitive quantification of dependence between two regions, such as the Pearson correlation or partial correlation. These approaches do not consider the spatiotemporal noise or voxel level fluctuations that are inherent to the BOLD signals (Achard and Gannaz, 2019).

In brain activation studies, as opposed to connectivity studies, spatial and spatiotemporal models have already been proposed to quantify brain regions activated under a certain task (Taylor and Worsley, 2007; Bowman, 2007). These models have been applied in fMRI (McIntosh, Chau and Protzner, 2004; Woolrich et al., 2004; Zhang et al., 2014), but are not directly applicable for constructing a single brain network from an individual scan taken at rest, which is the goal of this paper. As motivation, we will use an anatomical parcellation of a rat brain that contains 51 regions, with the aim to quantify and parameterize regional functional connectivity within a model for voxel-level signals to separately construct an individual brain network from each rat's fMRI scan. This will allow us to give an estimate of the classically defined *inter-regional*, or *long-range* connectivity network. Another key measurement of connectivity, termed the *intra-regional* connectivity, measures the dependence within a particular brain region. While we will emphasize estimation of inter-regional connectivity, as it is of primary interest in a large body of neuroimaging studies (Eickhoff, Yeo and Genon, 2018; Moghimi et al., 2022), intra-regional connectivity will play a key role in the estimation process.

With this purpose in mind, we highlight the main contributions of this paper. First, we propose a novel spatiotemporal statistical model for the BOLD signals at the voxel level. In principle, the collection of BOLD signals is considered to be a realization of a spatiotemporal process with a carefully designed covariance structure that explicitly models the different sources of variability leading to spatiotemporal dependency of the fMRI BOLD signals. The inter-regional connectivity between two arbitrary regions is quantified by a primal model parameter, which needs to be estimated along with a collection of auxiliary parameters that characterize the contributions of other underlying variability sources. The model will be presented in relatively general terms, after which an inferential pipeline will be developed in the

Gaussian setting. As a second main contribution, we devise an efficient two-stage strategy to estimate model parameters as computations associated with Gaussian processes are usually prohibitive. In particular, the proposed approach leverages large scale parallel computing with GPU accelerated matrix operations. In addition, we outline a justification for the use of large sample properties of the inter-regional connectivity estimates to provide sampling error quantification for network construction.

The remainder of the paper is arranged as follows. In Section 2, we present the model construction, parameterization, and estimation procedure. In particular, we propose the two-stage estimation procedure in Section 2.3. Assumptions and results on the asymptotic behavior of the estimators are presented in Section 2.4. Section 3 provides a set of simulation studies that demonstrates the empirical performance of our estimators on synthetic data. In Section 4, our model is applied to real rat data sets and brain connectivity is quantified using the new estimation procedure and standard errors provided by the asymptotic theory. Section 5 provides a discussion of the results and potential extensions.

2. Methodology. For an individual brain volume, let $\mathcal{B} \subset \mathbb{R}^3$ denote the connected set of spatial coordinates which is to be sampled. \mathcal{B} is divided into spatially disjoint and contiguous regions \mathcal{R}_j , $j = 1, \dots, J$, that is, $\mathcal{B} = \cup_{j=1}^J \mathcal{R}_j$ and $\mathcal{R}_j \cap \mathcal{R}_{j'} = \emptyset$, $j \neq j'$. Typically, studies of resting-state functional connectivity take a network-based approach to model the functional connectivity properties of the brain. In this network, the nodes correspond to the different brain regions \mathcal{R}_j , while connections between regions are determined by a collection of unknown parameters $\rho_{jj'}$, $1 \leq j < j' \leq J$, that are often taken to be correlation values. For now, let us assume that $|\rho_{jj'}| \leq 1$ represent correlations, so that we are dealing with a correlation network; that is, the edges may be considered binary according to whether $\rho_{jj'} = 0$, in which case there is no edge, or $\rho_{jj'} \neq 0$, indicating the presence of an edge between regions j and j' . Alternatively, the raw value $\rho_{jj'}$ can represent the strength of the edge between these regions in a weighted network.

In principle, brain activity evolves over a continuum, though it is not observed directly, continuously, or cleanly. Hence, to begin, denote by $Y_j(v, t)$ a latent BOLD signal at location $v \in \mathcal{R}_j$, $j = 1, \dots, J$, and at time $t \in [0, \mathcal{T}]$, where \mathcal{T} is the duration of the fMRI scan. The observed data are

$$(2.1) \quad X_{jlm} = Y_j(v_{jl}, t_m) + \epsilon_{jlm},$$

being sampled on a grid of voxels $v_{jl} \in \mathcal{R}_j$, $1 \leq l \leq L_j$, and a sequence of time points $0 = t_0 < t_1 < \dots < t_M = \mathcal{T}$, where ϵ_{jlm} are assumed to be independent and identically distributed zero-mean additive errors with variance σ^2 . At this point, it should be emphasized that, without further assumptions and modeling, a principled approach to statistical inference to reconstruct a network from the data would be difficult to justify, even if the latent processes $Y_j(v, t)$ were available to the scientist. This is due to the disparity between the resolution of the data, measured at unique voxels, and the parameters that are specified at the regional level. Put another way, the role of $\rho_{jj'}$, a regional parameter, on the joint distribution of the spatiotemporal fields Y_j and $Y_{j'}$ is not yet specified. Nevertheless, it has become commonplace in neuroscience to construct a network using the so-called ‘‘correlation of averages’’ that will be described next, along with an analysis of its statistical properties under a basic preliminary model for the fields Y_j .

2.1. Correlation of Averages. For a pair of regions, the common approach to quantify an empirically-based network is to first average voxel-level signals across space to obtain a mean signal for each region, that is,

$$(2.2) \quad \bar{X}_{jm} = L_j^{-1} \sum_{l=1}^{L_j} X_{jlm}.$$

The use of a single signal per region simplifies not only calculations by reducing the data dimension, but also the modeling that is required, since voxel-specific fluctuations are not taken into account. Letting $\tilde{\mu}_j$ and $\tilde{\zeta}_j^2$ be the empirical mean and variance of \bar{X}_{jm} across m (time), the usual Pearson correlation type quantification of connectivity is

$$(2.3) \quad \hat{\rho}_{jj'}^{\text{CA}} = \frac{M^{-1} \sum_{m=1}^M (\bar{X}_{jm} - \tilde{\mu}_j) (\bar{X}_{j'm} - \tilde{\mu}_{j'})}{\tilde{\zeta}_j \tilde{\zeta}_{j'}}.$$

We term the estimator in (2.3) the ‘‘correlation of averages’’ estimator as it averages signals by regions prior to the calculation of the Pearson correlation. Although this estimator is commonly used, only recently has more rigorous attention been given to the corresponding estimand. Ignoring the contribution of noise, which is somewhat mitigated by the averaging operation if the number of voxels is large, (2.3) would be a reasonable estimator if one assumes the correlation between two average regional signals is constant in time. Indeed, in those examples in the literature where a theoretical analysis of $\hat{\rho}^{\text{CA}}$ is provided, said analysis is typically done under the hypothetical framework of a single signal observed per region (Afyouni, Smith and Nichols, 2019; Azevedo et al., 2022), so that averaging across voxels is merely viewed as a preprocessing step without assessing the additional uncertainty that it induces. However, it is not clear what, if any, model imposed on the observed, voxel-level data would be consistent with this assumption.

To provide an initial and rudimentary analysis of this estimator for data at the voxel level, Achard et al. (2011) considered a model¹ for the Y_j as jointly Gaussian random fields with $\text{Corr}(Y_j(v, t), Y_{j'}(w, t)) = \rho_{jj'}^*$ for all $(v, w) \in \mathcal{R}_j \times \mathcal{R}_{j'}$ and $t \in [0, \mathcal{T}]$. That is, the correlation between latent signals observed simultaneously at any pair of spatial indices (v, w) is constant for each pair of regions. This is a natural way to generalize the role of the region-level correlation parameter to be homogeneous across different voxels, as it treats these as exchangeable, though not independent. Note that this correlation $\rho_{jj'}^*$ may differ from the aforementioned parameter $\rho_{jj'}$, as will now be elucidated.

Let us further suppose that $\xi_j^2 = \text{Var}(Y_j(v, t))$ for all $v \in \mathcal{R}_j$ and $t \in [0, \mathcal{T}]$. Then the analysis of Achard et al. (2011) shows that

$$(2.4) \quad \text{Corr}(\bar{X}_{jm}, \bar{X}_{j'm}) = \frac{\rho_{jj'}^*}{\sqrt{(\alpha_j + \beta_j)(\alpha_{j'} + \beta_{j'})}},$$

where $\alpha_j = L_j^{-2} \sum_{l, l'=1}^{L_j} \text{Corr}(Y_j(v_{jl}, t_m), Y_j(v_{j'l'}, t_m))$ is the average of all pairwise intra-regional correlations for region j and $\beta_j = \sigma^2 / (L_j \xi_j^2)$ can be considered as the noise-to-signal ratio. Hence, under mild assumptions on the temporal dependence, $\hat{\rho}^{\text{CA}}$ will converge almost surely to the right-hand side of (2.4) as the duration \mathcal{T} of the scan expands and the number M of temporal observation points diverges. At least two important facts can be gleaned from (2.4): first, that $\hat{\rho}^{\text{CA}}$ can be extremely biased as an estimator of $\rho_{jj'}^*$, and second, that the correlation value targeted by $\hat{\rho}^{\text{CA}}$ is heavily influenced by strength of within-region correlations and the noise level. For instance, in an extreme scenario in which there is no noise and $\alpha_j \alpha_{j'}$ is small, one is forced to conclude that $\rho_{jj'}^*$ cannot be large.

Achard et al. (2011) proposed various corrections to $\hat{\rho}^{\text{CA}}$ to appropriately target the parameter $\rho_{jj'}^*$. However, this does not eliminate the constraints placed on $\rho_{jj'}^*$ by the intra-regional correlation parameter α_j and noise variance. These effects are somewhat unnatural, as the connectivity parameter should intuitively be intrinsic to the brain itself and not dependent

¹In fact, the model of Achard et al. (2011) was applied to the discretely observed signals, while we generalize it to the latent fields.

on the sampling scheme (via the spatially averaged intra-regional correlations) or noisy perturbations imposed by the machine. Moreover, this basic model has other inadequacies; for example, it is not clear what intra-regional correlation values are valid in the sense that they lead to a spatiotemporal covariance field that is positive semidefinite. In the next section, these technical difficulties will be resolved by formulating a linear mixed model for the voxel-wise fMRI signals that encapsulates the essence of this basic model while clearly distinguishing the various sources of inter- and intra-regional dependencies.

2.2. A BOLD Random Effects Model. From a statistical modeling perspective, it is natural to view the collection of signals in each region as a cluster that is, in some sense, homogeneous compared to signals from other regions. At the same time, there must be a common source of variability across different clusters in order to allow for correlation between brain regions. Thus, to account for different sources of variability that induce the characteristics observed in fMRI data of inter-regional dependence, intra-regional dependence, and noise, we propose to formulate a linear mixed effect model. Although a long-standing staple in statistic modeling (not to mention specific fields such as psychometrics, econometrics, and many others), to the knowledge of the authors, this basic approach has not been used to develop a systematic approach to individual brain resting-state functional connectivity estimation from voxel-level data.

Begin by assuming a basic linear model for the latent BOLD signals as

$$(2.5) \quad Y_j(v, t) = \mu_j + \eta_j(t) + \gamma_j(v, t), \quad v \in \mathcal{R}_j, \quad j = 1, \dots, J, \quad t \in [0, \mathcal{T}].$$

Here, μ_j is the deterministic mean signal, which will be assumed to be constant in time throughout, but may vary across regions. The process η_j is a common zero-mean signal that is shared by all voxels in a given region, and is treated as a random effect. This term represents the desired homogeneity of signals within each region, consistent with the characterization of connectivity found elsewhere (e.g., [Van Den Heuvel and Pol, 2010](#)). The zero-mean spatiotemporal process γ_j represents the voxel-specific variations from the regional signals that are correlated across both spatial and temporal domains. However, the spatial dependence of the fields γ_j is assumed to persist over a short distance; specifically, the fields for different regions are assumed to be uncorrelated. Thus, the dependence between random effects η_j of different regions characterizes inter-regional connectivity while also inducing intra-regional correlation, and the random perturbations from γ_j can be considered as voxel-level spatiotemporal fluctuations resulting in intra-regional correlations that are idiosyncratic to each brain region.

The assumed dependence structures for the latent random fields Y_j can be summarized as follows. First, we assume the collection of temporal regional signals $\{\eta_j : j = 1, \dots, J\}$ is uncorrelated with the voxel-specific spatiotemporal fluctuations $\{\gamma_j : j = 1, \dots, J\}$. Furthermore, the random fields γ_j and $\gamma_{j'}$ are uncorrelated whenever $j \neq j'$. The spatiotemporal covariance structures for η_j (across regions and time) and γ_j (within region and across time) can be generically modeled as follows. Let $\mathbf{R} = \{\rho_{jj'}\}_{j,j'=1}^J$ be a $J \times J$ positive definite correlation matrix, A_η and B_j be positive definite covariance kernels on $[0, \mathcal{T}]^2$, and C_j be a positive definite spatial correlation kernel on \mathcal{R}_j . Then the assumed covariance model for (2.5) is

$$(2.6) \quad \text{Cov}(\eta_j(t), \eta_{j'}(t')) = \rho_{jj'} A_\eta(t, t'), \quad \text{Cov}(\gamma_j(v, t), \gamma_j(v', t')) = B_j(t, t') C_j(v, v').$$

Due to the problem motivating the model in (2.5), the primary parameters of interest are contained in the correlation matrix \mathbf{R} , while all other components are viewed as auxiliary nuisance parameters.

We pause to remark that (2.5) can be viewed as a model for spatial functional data, for which significant work exists; see, for example, Delicado et al. (2010); Hörmann and Kokoszka (2011); Gromenko et al. (2012); French and Kokoszka (2021); Zhang and Li (2022); Yarger, Stoev and Hsing (2022). However, the usual treatment of the temporal aspect of spatially-indexed functional data does not align particularly well with fMRI data. Spatial functional data methods typically assume a fixed compact domain $[0, \mathcal{T}]$ with increasingly dense observations t_m while, as a practical matter, one is forced to expand the domain $[0, \mathcal{T}]$ in order to obtain further temporal measurements of the fMRI signal. In addition, the spatial observation grid is essentially fixed for an fMRI scan, so that even in-fill spatial asymptotics are not appropriate. Spatial functional data models are also typically nonparametric to allow maximum flexibility, while the goal of functional connectivity estimation is to infer the inter-regional correlation parameters, so that nonparametric modeling may be unnecessary and even inefficient. Finally, tasks such as smoothing and kriging that are staples in functional methods do not directly address the matter at hand.

Combining (2.1) and (2.5), we obtain

$$(2.7) \quad X_{jlm} = \mu_j + \eta_{jm} + \gamma_{jlm} + \epsilon_{jlm},$$

where $\eta_{jm} = \eta_j(t_m)$ and $\gamma_{jlm} = \gamma_j(v_{jl}, t_m)$, $1 \leq l \leq L_j$, $1 \leq j \leq J$, $1 \leq m \leq M$ are the random effects, μ_j is the fixed effect, and ϵ_{jlm} are errors independent across all indices. Moreover, $\text{Cov}(\gamma_{jlm}, \gamma_{j'l'm'}) = 0$ whenever $j \neq j'$ and $\text{Cov}(\eta_{jm}, \gamma_{j'l'm'}) = 0$ for all possible indices. These various effects can be practically interpreted as follows. μ_j is an overall signal level related to the neurophysiological behavior during rest, η_{jm} are random regional effects that characterize the long-range, inter-regional connectivity that is the target of brain functional connectivity studies, γ_{jlm} represent local variations in blood flow that induce further correlated behavior between signals that are measured closely in time and space, and ϵ_{jlm} represent additional noise inherent to the scanner or other external sources.

2.3. Model Estimation. The proposed model in (2.7) coherently incorporates the inter-regional functional connectivity parameters $\rho_{jj'}$ with the voxel-level resolution of the observed data, all while allowing for heterogeneous intra-regional correlation behavior as well as noise, thus providing a promising foundation for voxel-level assessment of regional functional connectivity. One can approach estimation in a variety of ways, depending on further assumptions placed on the various effects. In this paper, we will illustrate the utility of (2.1) in the basic Gaussian setting, i.e., by assuming that the random components have a joint Gaussian distribution, and by placing stationary structures on the temporal and spatial covariance kernels. Specifically, for the functions in (2.6), we assume that A_η and B_j are temporally stationary covariance kernels, while C_j is a spatially stationary correlation kernel. That is, with $\delta_{ab} = \mathbf{1}(a = b)$ and $\|\cdot\|_2$ denoting the Kronecker delta and Euclidean norm, respectively,

$$(2.8) \quad \begin{aligned} A_\eta(t, t') &= k_\eta G(|t - t'|; \tau_\eta) + \sigma_\eta^2 \delta_{tt'}, \\ B_j(t, t') &= k_{\gamma_j} H_j(|t - t'|; \tau_{\gamma_j}), \\ C_j(v, w) &= K_j(\|v - w\|_2; \phi_{\gamma_j}), \end{aligned}$$

for valid stationary correlation kernels G, H_j , and K_j defined on the non-negative real line, and variances $k_\eta, k_{\gamma_j}, \sigma_\eta^2 > 0$, where the kernels are assumed to be known up to the rate parameters $\tau_\eta, \tau_{\gamma_j}, \phi_{\gamma_j} > 0$, $j = 1, \dots, J$. We model the covariance structure of η_j with a nugget effect σ_η^2 to allow for short-scale variability that is under the measurement unit of t . Numerically, this nugget effect also serves to stabilize the estimation as the gradient of $\rho_{jj'}$ is tied to that of $A_\eta(t, t')$, and small values of k_η could result in large variability in the estimated $\rho_{jj'}$ if such a nugget effect is not present.

Suppose now that $\{(\eta_1(t), \dots, \eta_J(t)) : t \in [0, \mathcal{T}]\}$ is a multivariate Gaussian process, $\gamma_1, \dots, \gamma_J$ are independent Gaussian spatiotemporal random fields, and $\epsilon_{ljm} \stackrel{\text{iid}}{\sim} \mathbf{N}(0, \sigma^2)$. Then (2.8) implies that (2.7) is a Gaussian linear mixed effect model. However, as Gaussian likelihood usually requires, with $n = M \sum_{j=1}^J L_j$ being the total number of data points, $O(n^3)$ computing time and $O(n^2)$ memory, the large size of the data set usually makes a straight shot at likelihood evaluation prohibitive. For context, a typical human fMRI scan consists of a voxel count on the order of 10,000 with M on the order of 100, while the corresponding parameters for a rate are around 3000 voxels and a few hundred timepoints. Therefore, we will endeavor to break down the computation into smaller, simpler pieces. In doing so, we will also draw a connection to the usual estimator $\hat{\rho}^{\text{CA}}$ in the context of this model, and propose two new alternative functional connectivity estimators.

As a full maximum likelihood approach is prohibitive, we will restrict our attention to individual pairs of regions, motivated by the position of the correlation $\rho_{jj'}$ as the primary parameters of interest. Specifically, we propose a two-stage estimation approach. In the first step, one isolates data for each region in order to estimate the covariance parameters associated with the intra-regional spatiotemporal noise γ_j . In the second step, one isolates each pair of regions in order to estimate the remaining parameters, which include the inter-regional correlations.

2.3.1. *Stage 1: Estimating Region-Specific Parameters.* In the first step, one considers all data for each region \mathcal{R}_j individually. A benefit of this approach is that all regional parameters

$$(2.9) \quad \boldsymbol{\theta}_j = \{\phi_{\gamma_j}, k_{\gamma_j}, \tau_{\gamma_j}\}$$

can be estimated in parallel. At this stage, all signals within a same region have a common component signal that is a single realization of η_j , which will be treated as a fixed effect. In other words, we will condition the observed data on the unobserved latent process η_j , and maximize the conditional likelihood. The *intra-regional* model of the observed BOLD signals, conditional on $\boldsymbol{\eta}_j = (\eta_{j1}, \dots, \eta_{jM})$, is

$$(2.10) \quad \bar{X}_{jlm} \mid \boldsymbol{\eta}_j = \nu_{jlm} + \gamma_{jlm} + \epsilon_{jlm}, \quad \nu_{jlm} = \mu_j + \eta_{jlm}.$$

Note that, since the spatiotemporal noise γ_j and measurement errors are assumed to be independent of η_j , their variance components are not affected by conditioning. Thus, the sole effect of conditioning on η_j is to treat it as a fixed effect in the first step of estimation. There are two reasons for doing this, one practical and the other computational. As a practical matter, by estimating the regional effects ν_{jlm} as a single fixed effect, one mimics the first step in the Correlation of Averages estimator outlined in Section 2.1. Indeed, if one assumes independence in both time and space, \bar{X}_{jlm} in (2.2) would be the maximum likelihood estimator of ν_{jlm} . However, under dependence, the Correlation of Averages approach will be less efficient, though computationally simpler, as an estimator of ν_{jlm} , since it does not account for any spatiotemporal dependencies. The conditional treatment of η_j also has computational advantages associated with the use of a Gaussian likelihood, as it renders a Kronecker covariance structure that enables faster computation of inverse covariance matrices that would not be possible to exploit if treating η_j as a random effect in *Stage 1*.

Because the number of fixed effects now scales with the number time points M , we reduce the dimension of the problem by using a B-spline basis expansion. In terms of the neuroscience problem at hand, this implies that the underlying latent signals that embody the collaborative operation of distinct brain regions possesses some degree of smoothness, which is an intuitive assumption. Specifically, suppose $\{\psi_k\}_{k=1}^K$ is a cubic B-spline basis on a given set of interior knots $\{s_u\}_{u=1}^{K-4}$. Then we approximate the fixed effects by

$\nu_{jm} \approx \sum_{k=1}^K v_{jk} \psi_k(t_m)$. Let $\mathbf{v}_j = [v_{j1}, \dots, v_{jK}]^\top$. An initial estimate of the fixed effect represented by \mathbf{v}_j can be obtained by fitting a regression spline on the sample pairs $\{t_m, X_{jlm}\}$, $l = 1, \dots, L_j$, $m = 1, \dots, M$, which yields $\hat{\mathbf{v}}_j$. This estimate can either be fixed throughout the minimization of the negative likelihood function, or simply be used as a starting point that is updated along with the variance components.

For $j = 1, \dots, J$, denote the observed signals for region \mathcal{R}_j by

$$(2.11) \quad \mathbf{X}_j = [X_{j11}, X_{j12}, \dots, X_{j1M}, X_{j21}, \dots, X_{jL_j M}]^\top,$$

which is a column vector of stacked BOLD signals. Similarly, set

$$(2.12) \quad \begin{aligned} \boldsymbol{\gamma}_j &= [\gamma_{j11}, \gamma_{j12}, \dots, \gamma_{j1M}, \gamma_{j21}, \dots, \gamma_{jL_j M}]^\top, \\ \boldsymbol{\epsilon}_j &= [\epsilon_{j11}, \epsilon_{j12}, \dots, \epsilon_{j1M}, \epsilon_{j21}, \dots, \epsilon_{jL_j M}]^\top. \end{aligned}$$

Define the matrix

$$(2.13) \quad \tilde{\mathbf{G}} = \begin{bmatrix} \psi_1(t_1) & \psi_2(t_1) & \dots & \psi_K(t_1) \\ \psi_1(t_2) & \psi_2(t_2) & \dots & \psi_K(t_2) \\ \vdots & \vdots & \ddots & \vdots \\ \psi_1(t_M) & \psi_2(t_M) & \dots & \psi_K(t_M) \end{bmatrix},$$

and $\mathbf{G} = \mathbf{1}_{L_j} \otimes \tilde{\mathbf{G}}$, where \otimes denotes the Kronecker product and $\mathbf{1}_{L_j}$ is the column vector of 1's with length L_j . Then the matrix form of (2.10) is

$$(2.14) \quad \mathbf{X}_j \mid \boldsymbol{\eta}_j = \mathbf{G}_j \mathbf{v}_j + \boldsymbol{\gamma}_j + \boldsymbol{\epsilon}_j.$$

Looking ahead, in order to estimate the regional parameters (2.9) in this model, we construct and solve for restricted maximum likelihood (ReML) problem, or equivalently, minimize the negative value of the restricted log likelihood function of $\mathbf{X}_j \mid \boldsymbol{\eta}_j$. The reason that we prefer ReML over the usual maximum likelihood (ML) is because ReML yields asymptotically unbiased estimators for the covariance components by fitting likelihood based on a set of contrasts that eliminates the fixed effects (Harville, 1974; Jennrich and Schluchter, 1986; Lindstrom and Bates, 1988; Pinheiro and Bates, 2006). We note that it is feasible and reasonable to recover the fixed effects from ReML estimates. However, the caveat is that the ReML estimated fixed effects are not invariant under change of basis of data, which is a desired property possessed by the usual ML estimators (see Pinheiro and Bates, 2006, page 76). It is clear that the ReML function includes the variance of measurement errors σ^2 , which enters the covariance matrix diagonally in an additive manner. If one factors out σ^2 from the entire covariance structure of $\mathbf{X}_j \mid \boldsymbol{\eta}_j$, $\hat{\sigma}^2$ can be analytically represented by the other parts of the likelihood function, which makes the computation process faster and more accurate; see (2.18) and (2.26).

Provided that one uses the analytical solution for $\hat{\sigma}^2$, the model parameter estimates are invariant to the choice between estimating k_{γ_j} directly, or estimating the variance ratio $\tilde{k}_{\gamma_j} = k_{\gamma_j} / \sigma^2$, as a whole. We adopt the latter approach for improved computation efficiency. Indeed, one can observe that the estimation of the primary parameters $\rho_{jj'}$ only requires estimating the variance ratios of the model components. Therefore, letting $\{\tilde{\mathbf{B}}_j\}_{mm'} = \tilde{B}_j(t_m, t_{m'}) = \tilde{k}_{\gamma_j} H_j(t_m, t_{m'}; \tau_{\gamma_j})$, $\{\mathbf{C}_j\}_{lw} = K_j(\|v_{jl} - v_{jw}\|_2; \phi_{\gamma_j})$, and \mathbf{I}_A be the $A \times A$ identity matrix, the marginal model of (2.10) is

$$(2.15) \quad \mathbf{X}_j \sim \mathbf{N}(\mathbf{G}_j \mathbf{v}_j, \sigma^2 \mathbf{V}_j(\boldsymbol{\theta}_j)),$$

where

$$(2.16) \quad \mathbf{V}_j(\boldsymbol{\theta}_j) = \mathbf{C}_j \otimes \tilde{\mathbf{B}}_j + \mathbf{I}_{(ML_j)}.$$

Suppressing dependence of V_j on θ_j , the corresponding negative ReML function is

$$(2.17) \quad \begin{aligned} \mathcal{L}_j^{\text{ReML}}(\mathbf{v}_j, \theta_j | \mathbf{X}_j, \boldsymbol{\eta}_j) &= \frac{1}{2} \log |\mathbf{V}_j| \\ &+ \frac{1}{2} \log \left| \mathbf{G}_j^\top \mathbf{V}_j^{-1} \mathbf{G}_j \right| \\ &+ \frac{1}{2} (ML_j - K) \log (\mathbf{X}_j - \mathbf{G}_j \mathbf{v}_j)^\top \mathbf{V}_j^{-1} (\mathbf{X}_j - \mathbf{G}_j \mathbf{v}_j), \end{aligned}$$

where σ^2 has been profiled using

$$(2.18) \quad \sigma^2 = \frac{1}{L_j M - K} (\mathbf{X}_j - \mathbf{G}_j \mathbf{v}_j)^\top \hat{\mathbf{V}}_j^{-1} (\mathbf{X}_j - \mathbf{G}_j \mathbf{v}_j).$$

Estimating the regional covariance components θ_j by minimizing the negative ReML function in (2.17) is referred to as *Stage 1* estimation in our two-stage approach. In particular, $\hat{\theta}_j$ will be plugged into the full ReML function in *Stage 2* (see Section 2.3.2, where it can be further updated or held fixed to reduce computation cost. The estimated parameters for fixed effects \hat{v}_j obtained by B-Spline regression are used as the initial values of the optimization. In the case where one updates these estimates, the analytical generalized least square (GLS) estimator should be used rather than running the optimizer on \mathbf{v}_j directly, that is, $\hat{v}_j = (\mathbf{G}_j^\top \hat{\mathbf{V}}_j^{-1} \mathbf{G}_j)^{-1} \mathbf{G}_j^\top \hat{\mathbf{V}}_j^{-1} \mathbf{X}_j$. The Kronecker structure of the covariance matrix in (2.16) allows us to use scalable inference approaches as shown in Saatchi (2011). See Section A.1 of Appendix A for details on this scalable inference approach, including Algorithm 1 that details the optimization steps.

As mentioned previously, a modified version of the correlation of averages estimator might also be considered at the end of *Stage 1*. Recall that one obtains the fixed-effects estimates in *Stage 1* as

$$(2.19) \quad \hat{v}_{jm} = \sum_{k=1}^K \hat{v}_{jk} \psi_k(t_m), \quad j = 1, \dots, L_j, m = 1, \dots, M.$$

Then, letting $\check{\mu}_j$ and $\check{\zeta}_j^2$ be the empirical mean and variance of \hat{v}_{jm} across m (time), this modified estimator of $\rho_{jj'}$ is

$$(2.20) \quad \tilde{\rho}_{jj'}^{\text{CA}} = \frac{M^{-1} \sum_{m=1}^M (\hat{v}_{jm} - \check{\mu}_j)(\hat{v}_{j'm} - \check{\mu}_{j'})}{\check{\zeta}_j \check{\zeta}_{j'}}.$$

This estimator will be similar to the correlation of averages when the number of knots is large (close to M) and the estimate of \mathbf{v}_j is computed only using the initial spline computation, without updating it in the likelihood maximization step.

2.3.2. Stage 2: Estimating Global and Inter-Regional Parameters. Having obtained estimates for the regional variance components in *Stage 1*, we advance to pairwise regional data. Without loss of generality, consider regions $\mathcal{R}_1, \mathcal{R}_2$. Let $\mathbf{X} = [\mathbf{X}_1^\top, \mathbf{X}_2^\top]^\top$, $\boldsymbol{\mu} = [\mu_1, \mu_2]^\top$, $\boldsymbol{\eta} = [\boldsymbol{\eta}_1^\top, \boldsymbol{\eta}_2^\top]^\top$, $\boldsymbol{\gamma}^\top = [\boldsymbol{\gamma}_1^\top, \boldsymbol{\gamma}_2^\top]^\top$, $\boldsymbol{\alpha} = [\boldsymbol{\eta}^\top, \boldsymbol{\gamma}^\top]^\top$, and $\boldsymbol{\epsilon} = [\boldsymbol{\epsilon}_1^\top, \boldsymbol{\epsilon}_2^\top]^\top$. Furthermore, define the design matrices

$$\mathbf{Z} = \begin{bmatrix} \mathbf{1}_{ML_1} & \mathbf{0}_{ML_1} \\ \mathbf{0}_{ML_2} & \mathbf{1}_{ML_2} \end{bmatrix},$$

and $\mathbf{U} = [\mathbf{Z}, \mathbf{I}_{M(L_1+L_2)}]$, where $\mathbf{0}_L$ is the column vector of 0's of length L . Then the pairwise *inter-regional* model has the matrix form

$$(2.21) \quad \mathbf{X} = \mathbf{Z}\boldsymbol{\mu} + \mathbf{U}\boldsymbol{\alpha} + \boldsymbol{\epsilon}.$$

Following the discussion under (2.10), define $\tilde{k}_\eta = k_\eta/\sigma^2$, $\tilde{\sigma}_\eta^2 = \sigma_\eta^2/\sigma^2$, and $\{\tilde{\mathbf{A}}\}_{t_m t_{m'}} = \tilde{A}_\eta(t_m, t_{m'}) = \tilde{k}_\eta G(|t_m - t_{m'}|; \tau_\eta) + \tilde{\sigma}_\eta^2 \delta_{mm'}$. Let $\boldsymbol{\theta}$ be the vector of parameters that characterizes the covariance structure of \mathbf{X} , which is a superset of the regional parameter vectors $\boldsymbol{\theta}_1, \boldsymbol{\theta}_2$, given by

$$(2.22) \quad \boldsymbol{\theta} = [\tau_\eta, k_\eta, \phi_{\gamma_1}, \phi_{\gamma_2}, \tilde{\tau}_{\gamma_1}, \tilde{k}_{\gamma_1}, \tilde{\tau}_{\gamma_2}, \tilde{k}_{\gamma_2}, \rho_{12}, \tilde{\sigma}_\eta^2]^\top.$$

Then, the corresponding marginal model is

$$(2.23) \quad \mathbf{X} \sim \mathbf{N}(\mathbf{Z}\boldsymbol{\mu}, \sigma^2 \mathbf{V}(\boldsymbol{\theta})),$$

where

$$(2.24) \quad \mathbf{V}(\boldsymbol{\theta}) = \begin{bmatrix} \mathbf{C}_1 \otimes \tilde{\mathbf{B}}_1 + \mathbf{J}_{L_1, L_1} \otimes \tilde{\mathbf{A}} & \rho_{12} \mathbf{J}_{L_1, L_2} \otimes \tilde{\mathbf{A}} \\ \rho_{12} \mathbf{J}_{L_2, L_1} \otimes \tilde{\mathbf{A}} & \mathbf{C}_2 \otimes \tilde{\mathbf{B}}_2 + \mathbf{J}_{L_2, L_2} \otimes \tilde{\mathbf{A}} \end{bmatrix} + \mathbf{I}_{M(L_1+L_2)}$$

and $\mathbf{J}_{L, L'}$ is the $L \times L'$ matrix of 1's. To simplify the notation, we will reduce $\mathbf{V}(\boldsymbol{\theta})$ to \mathbf{V} . One can estimate the model parameters $\boldsymbol{\theta}, \boldsymbol{\mu}$ by minimizing the negative value of the ReML function for inter-regional model, given by

$$(2.25) \quad \begin{aligned} \mathcal{L}^{\text{ReML}}(\boldsymbol{\mu}, \boldsymbol{\theta} \mid \mathbf{X}) &= \frac{1}{2} \log |\mathbf{V}| \\ &+ \frac{1}{2} \log |\mathbf{Z}^\top \mathbf{V}^{-1} \mathbf{Z}| \\ &+ \frac{1}{2} (M(L_1 + L_2) - 2) \log (\mathbf{X} - \mathbf{Z}\boldsymbol{\mu})^\top \mathbf{V}^{-1} (\mathbf{X} - \mathbf{Z}\boldsymbol{\mu}). \end{aligned}$$

The estimates from *Stage 1* can either be fixed throughout the optimization iterations, or be used as initial values for the full optimization procedure and updated during the optimization. Similar to *Stage 1*, $\hat{\boldsymbol{\mu}}$ is obtained by its generalized least squares (GLS) estimator. Again, profiling has been applied via

$$(2.26) \quad \sigma^2 = \frac{1}{M(L_1 + L_2) - 2} (\mathbf{X} - \mathbf{Z}\boldsymbol{\mu})^\top \mathbf{V}^{-1} (\mathbf{X} - \mathbf{Z}\boldsymbol{\mu}).$$

We refer the estimation of $\boldsymbol{\theta}$ as *Stage 2* of our two-stage approach, and denote the estimated correlation parameter as $\hat{\rho}_{12}^{\text{ReML}}$. While the covariance matrix in (2.24) no longer possesses the Kronecker structure from *Stage 1*, we exploit its block structure by using the Schur complement (Petersen and Pedersen, 2008) to efficiently compute inverses when evaluating the loss function in (2.25). Details are included in Section A.2 of Appendix A, including the computational details in Algorithm 2.

In our experiments in Sections 3 and 4, two optimizers were investigated to carry out the two-stage estimation approach. The first one is the gradient based limited-memory-Broyden-Fletcher-Goldfarb-Shanno (LBFGS) solver (Nocedal, 1980), which is a widely adapted optimizer that implements a quasi-Newton method. By leveraging an approximate Hessian matrix, this method provides an optimization algorithm that is efficient in both time and memory. The potential pitfall is that the method can become unstable if elements of the gradient become small. To mitigate this issue, we also used a trust region based optimizer, the bound-optimization-by-quadratic-approximation (BOBYQA) solver (Powell, 2009). Although slower than a gradient-based optimizer, this derivative-free algorithm was found to be more stable in our experiments on real data. As a result, we use the LBFGS optimizer in the simulation studies for its efficiency and BOBYQA in real data application for its stability.

2.4. *Asymptotic Inference for $\hat{\rho}^{\text{ReML}}$ estimators.* Another advantage of the proposed model is that the influence of the spatiotemporal dependence between the various signals can be incorporated into the assessment of estimation uncertainty by using well-established asymptotic properties of ReML estimators. In keeping with the nature of fMRI data, the appropriate asymptotic regime is that of an expanding time window \mathcal{T} , with the number of time measurements M diverging accordingly. While the spatial dimensions, or region sizes, remain fixed, we remark that these still plays a crucial role since the spatial design is not a regular lattice and the spatial correlation is only assumed to be stationary within a region and not across the entire brain. General asymptotic properties for ReML estimators under the spatial regression setting were investigated by [Cressie and Lahiri \(1993\)](#) in which the main focus was on the parameters of the residual covariance structure, matching the focus of our motivating problem. [Cressie and Lahiri \(1996\)](#) further proposed practically verifiable sufficient conditions for the asymptotic results of ReML estimators to hold under various common settings.

For simplicity, as well as to be faithful to the computational approach outlined above, we always consider the pairwise model (2.21), so that the sample size is $n = M(L_1 + L_2)$ and the model parameters of interest is $\boldsymbol{\theta} \in \mathbb{R}^{10}$, defined in (2.22), which contains the key correlation parameter. Define

$$(2.27) \quad \boldsymbol{\Pi}(\boldsymbol{\theta}) = \mathbf{V}^{-1}(\boldsymbol{\theta}) - \mathbf{V}^{-1}(\boldsymbol{\theta})\mathbf{Z}(\mathbf{Z}^\top\mathbf{V}^{-1}(\boldsymbol{\theta})\mathbf{Z})^{-1}\mathbf{Z}^\top\mathbf{V}^{-1}(\boldsymbol{\theta}),$$

which is the projection of $\mathbf{V}^{-1}(\boldsymbol{\theta})$ onto the orthogonal complement column space of the design matrix \mathbf{Z} , arising from the ReML technique of removing the fixed effects. Let $\mathbf{V}_i(\boldsymbol{\theta}) = \partial\mathbf{V}(\boldsymbol{\theta})/\partial\theta_i$, where θ_i is the i th element of $\boldsymbol{\theta}$, $i = 1, \dots, 10$. Similarly, $\mathbf{V}_{ij}(\boldsymbol{\theta}) = \partial^2\mathbf{V}(\boldsymbol{\theta})/\partial\theta_i\partial\theta_j$, $i, j = 1, \dots, 10$. Furthermore, let $\mathcal{I}(\boldsymbol{\theta})$ be the $p \times p$ matrix of second-order partial derivatives of the negative ReML function, that is, $\{\mathcal{I}(\boldsymbol{\theta})\}_{ij} = \partial^2\mathcal{L}^{\text{ReML}}(\boldsymbol{\theta})/\partial\theta_i\partial\theta_j$, $1 \leq i, j \leq p$. It is straightforward to show that the ij th element of Fisher information matrix is

$$(2.28) \quad \mathbb{E}_{\boldsymbol{\theta}}(\mathcal{I}(\boldsymbol{\theta}))_{ij} = \frac{1}{2} \text{Tr} \{ \boldsymbol{\Pi}(\boldsymbol{\theta})\mathbf{V}_i(\boldsymbol{\theta})\boldsymbol{\Pi}(\boldsymbol{\theta})\mathbf{V}_j(\boldsymbol{\theta}) \}, \quad 1 \leq i, j \leq p.$$

Application of the results in Theorems 3.1 and 3.2 of [Cressie and Lahiri \(1993\)](#) to our setting is then relatively straightforward. As time is the only dimension that is involved in the asymptotic development, the assumptions used in [Cressie and Lahiri \(1993\)](#) to derive these results amount to restrictions in the temporal correlation decay represented by the matrices $\tilde{\mathbf{B}}_j$ and $\tilde{\mathbf{A}}$. When these are satisfied, one immediately finds that

$$(2.29) \quad \{\mathbb{E}\mathcal{I}_n(\boldsymbol{\theta})\}^{1/2} (\hat{\boldsymbol{\theta}}^{\text{ReML}} - \boldsymbol{\theta}) \rightsquigarrow \mathbf{N}(\mathbf{0}, \mathbf{I}_p),$$

with \rightsquigarrow denoting convergence in distribution. Focusing only on the primary parameter $\hat{\rho}^{\text{ReML}}$, a consequence of the above is that

$$(2.30) \quad \left\{ \frac{1}{2} \text{Tr} \left\{ \left(\boldsymbol{\Pi}(\boldsymbol{\theta}) \begin{bmatrix} \mathbf{0} & \mathbf{J}_{L_1, L_2} \\ \mathbf{J}_{L_2, L_1} & \mathbf{0} \end{bmatrix} \otimes \tilde{\mathbf{A}} \right)^2 \right\} \right\}^{\frac{1}{2}} (\hat{\rho}_{12}^{\text{ReML}} - \rho_{12}) \rightsquigarrow \mathbf{N}(\mathbf{0}, 1).$$

The standardizing matrix in (2.30) can be readily estimated by plugging in the relevant components of the computed estimate $\hat{\boldsymbol{\theta}}$ into $\boldsymbol{\Pi}(\boldsymbol{\theta})$ and $\tilde{\mathbf{A}}$.

3. Simulation Study. To understand the performance of our model, we proceed with a simulation study. We simultaneously simulate BOLD signals from 3 regions under different settings by varying signal strength and intra-regional correlation. For the temporal correlation

kernels G and H_j in (2.8), we use the squared exponential kernel (also called the Gaussian or radial basis function (RBF) kernel)

$$(3.1) \quad \kappa(u; \tau) = \exp\left(-\frac{\tau^2 u^2}{2}\right),$$

setting $G(u; \tau_\eta) = \kappa(u; \tau_\eta)$ and $H_j(u; \tau_{\gamma_j}) = \kappa(u; \tau_{\gamma_j})$. For the spatial correlation kernel K_j in (2.8), we used the Matérn-5/2 kernel

$$(3.2) \quad K_j(d; \phi_{\gamma_j}) = \left(1 + \sqrt{5}\phi_{\gamma_j}d + \frac{5}{3}\phi_{\gamma_j}^2 d^2\right) \exp\left(-\sqrt{5}\phi_{\gamma_j}d\right),$$

that is a popular choice in spatial statistics (Stein, 1999).

One of the main goals is to study the performance of our estimator $\hat{\rho}^{\text{ReML}}$ in comparison to $\hat{\rho}^{\text{CA}}$ under different settings of signal strength relative to spatiotemporal noise, which is mainly quantified by the values of \tilde{k}_η relative to those of \tilde{k}_γ . Therefore, we set $\tilde{k}_\gamma = 2$, $\tau_\gamma = 0.5$ for all regions and fix $\sigma^2 = 1$, $\tau_\eta = 0.25$, and $\tilde{\sigma}_\eta^2 = 0.1$ for all simulations. Additionally, we fix the mean signals to be $\mu_1 = 1, \mu_2 = 10, \mu_3 = 20$ and the pairwise inter-regional correlations are $\rho_{12} = 0.1, \rho_{13} = 0.35, \rho_{23} = 0.6$. For each setting, $Q = 100$ independent simulations were run with $L_j \equiv 50$ voxels for each region (randomly sampled from a 3D rectangular lattice with side length of 7) and $M = 60$ timepoints for all signals. In *Stage 1* estimation, $K = 45$ cubic B-spline basis functions were used to approximate the fixed effect using an equally spaced set of 41 interior knots. The code for all simulations can be found on Github (<https://github.com/cbtran/qfuncMM-reproducible>).

3.1. Comparison of estimators. First, we compare estimation performance of the three estimators, $\hat{\rho}^{\text{ReML}}$, $\hat{\rho}^{\text{CA}}$, and $\tilde{\rho}^{\text{CA}}$, which are the ReML estimator of ρ , the conventional Pearson correlation of averages (CA), and the Pearson correlation of averages on B-spline fixed effect estimates from *Stage 1* (FE), respectively. The calculation of the two correlation of averages type estimators are detailed in (2.3) and (2.20). Four settings were considered, corresponding to weak ($\phi_\gamma = 1$) and strong ($\phi_\gamma = 0.25$) intra-regional correlation and weak ($k_\eta = 0.5$) and strong ($k_\eta = 1$) signal.

The estimation performances of the different estimators under each setting are shown in Figure 1 and Table 1. Overall, $\hat{\rho}^{\text{ReML}}$ has the smallest standard deviation for all settings, which can be observed visually in Figure 1 and numerically in Table 1. In the case of weak intra-regional correlation ($\phi_\gamma = 1$), the true values of ρ are between the 1st and 3rd quartiles from all estimators. Notably, $\hat{\rho}^{\text{CA}}$ and $\tilde{\rho}^{\text{CA}}$ are biased toward 0, their medians deviating strongly from the true value when $\rho = 0.6$. Unsurprisingly, the effect of bias seems to be less severe when signal gets stronger ($k_\eta = 1$), resulting in better concentrations around the true value for both estimators. Similarly, $\hat{\rho}^{\text{CA}}$ and $\tilde{\rho}^{\text{CA}}$ are heavily biased towards 0 in the cases of strong intra-regional correlation ($\phi_\gamma = 0.25$). Especially when $\rho = 0.6$, their 3rd quartiles are smaller than the true value of inter-regional correlation. On the other hand, $\hat{\rho}^{\text{ReML}}$ is still robust with its median staying close to the true inter-regional correlations even though its spread increases. Interestingly, $\tilde{\rho}^{\text{CA}}$ seems to perform better than $\hat{\rho}^{\text{CA}}$ for strong intra-regional correlation and strong inter-regional correlation. This result suggests that our fixed-effect estimator \hat{v} from (2.19) might provide a better estimate for η_j signal than regional averages, particularly when data are not independent and identically distributed. Overall, we can observe that $\hat{\rho}^{\text{ReML}}$ is the most robust estimator across all different simulation settings. See Appendix B for additional simulation results with very strong signal ($k_\eta = 1.5$).

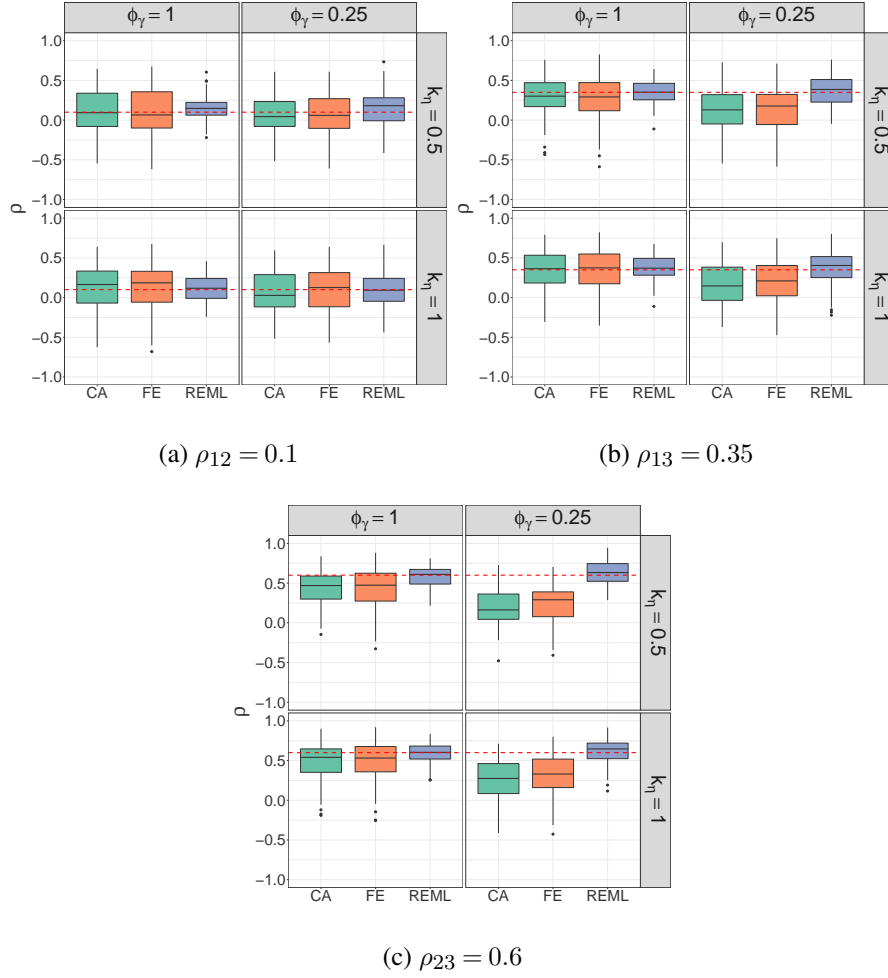


Fig 1: Empirical distribution of estimated inter-regional correlations: (a) Weak inter-regional correlation, (b) Medium inter-regional correlation, (c) Strong inter-regional correlation. In each subfigure, two intra-regional correlation rates are $\phi_\gamma = 0.25$ (strong) and $\phi_\gamma = 1$ (weak), and two levels of signal are $k_\eta = 0.5$ (weak) and $k_\eta = 1$ (strong). The three estimators are Pearson correlation of average (CA, $\hat{\rho}^{CA}$), Pearson correlation of fixed-effect estimate (FE, $\hat{\rho}^{FE}$), and the proposed ReML estimator (ReML, $\hat{\rho}^{ReML}$). Dashed line denotes the true value of inter-regional correlation.

3.2. *Validation of large sample properties.* Next, we validate the asymptotic normality of $\hat{\rho}^{ReML}$ from Theorem 2.30 by constructing confidence intervals. Using Fisher transformation, the $(1 - \alpha)$ confidence interval then has the form

$$(3.3) \quad C_{1-\alpha}^{ReML} = \tanh \left(\text{arctanh}(\hat{\rho}^{ReML}) \pm \Phi^{-1}(1 - \alpha/2) \times SE(\text{arctanh}(\hat{\rho}^{ReML})) \right),$$

where $\hat{\rho}^{ReML}$ is estimated correlation via ReML from Section 3.1, $SE(\text{arctanh}(\hat{\rho}^{ReML}))$ is the standard error of transformed parameter $\text{arctanh}(\hat{\rho}^{ReML})$ computed via the δ -method, and $\Phi^{-1}(\cdot)$ is the quantile function of the standard normal distribution.

The coverage of confidence intervals which is the percentage of intervals that cover the true inter-regional correlation for all 3 pairs at different significant levels α are shown Figure 2. Similar to estimation results, confidence intervals get better coverage as signal strength increases and intra-regional correlation decreases. When intra-regional correlation is strong ($\phi_\gamma = 0.25$), confidence intervals failed to achieve the desired $1 - \alpha$ coverage with all lines

TABLE 1

Estimates of correlation coefficients from simulated data. Two levels of intra-regional correlation, $\phi_\gamma = 0.25$ (strong) and $\phi_\gamma = 1$ (weak), and three levels of inter-regional correlation, $\rho = 0.1, 0.35, 0.6$, and two levels of signal strength $k_\eta = 0.5, 1$ are used. The three estimators are Pearson correlation of average (CA, $\hat{\rho}^{CA}$), Pearson correlation of fixed-effect estimate (FE, $\hat{\rho}^{CA}$), and the proposed ReML estimator (ReML, $\hat{\rho}^{ReML}$).

Signal	Intra-correlation	ρ_{True}	Type	RMSE	Bias	SD
$k_\eta = 0.5$	$\phi_\gamma = 1$	0.1	ReML	0.1584	0.0379	0.1546
			FE	0.3145	0.0101	0.3159
			CA	0.2793	0.0044	0.2806
		0.35	ReML	0.1387	0.0057	0.1393
			FE	0.2925	0.0640	0.2869
			CA	0.2606	0.0576	0.2555
	0.6	ReML	0.1231	0.0105	0.1232	
		FE	0.2904	0.1587	0.2444	
		CA	0.2645	0.1595	0.2121	
	$\phi_\gamma = 0.25$	0.1	ReML	0.2255	0.0474	0.2216
			FE	0.2638	0.0205	0.2643
			CA	0.2271	0.0344	0.2256
0.35		ReML	0.1897	0.0136	0.1902	
		FE	0.3537	0.2187	0.2793	
		CA	0.3532	0.2321	0.2677	
0.6	ReML	0.1550	0.0247	0.1538		
	FE	0.4246	0.3547	0.2346		
	CA	0.4701	0.4132	0.2254		
$k_\eta = 1$	$\phi_\gamma = 1$	0.1	ReML	0.1638	0.0133	0.1641
			FE	0.3104	0.0361	0.3098
			CA	0.2897	0.0263	0.2900
		0.35	ReML	0.1593	0.0181	0.1591
			FE	0.2641	0.0032	0.2654
			CA	0.2445	0.0093	0.2455
	0.6	ReML	0.1309	0.0147	0.1307	
		FE	0.2765	0.1057	0.2568	
		CA	0.2602	0.1108	0.2366	
	$\phi_\gamma = 0.25$	0.1	ReML	0.2113	0.0034	0.2124
			FE	0.3012	0.0100	0.3026
			CA	0.2670	0.0306	0.2666
0.35		ReML	0.2083	0.0235	0.2080	
		FE	0.2996	0.1393	0.2666	
		CA	0.3153	0.1803	0.2600	
0.6	ReML	0.1604	0.0178	0.1602		
	FE	0.3917	0.2868	0.2681		
	CA	0.4222	0.3345	0.2589		

are under the reference $y = x$ line. This result is unsurprising since in the presence of strong intra-regional correlations among voxels, effective sample size decreases, thus more samples are needed for the large sample properties to be satisfied.

4. Data Application. Having demonstrated the robust empirical performance of the proposed estimator $\hat{\rho}^{\text{ReML}}$ in simulation studies, we proceed to the motivating data application. The model was applied to one dead and one anesthetized live rat. These data sets, among others, have been previously described and studied in [Becq et al. \(2020\)](#). In particular, the live rat under analysis in this paper is labeled as rat 20160616_145220 whose BOLD signals were collected after administration of the Etomidate anesthetic. The dead rat analyzed is labeled as rat 0160524_153000 and is used primarily to illustrate performance of the model estimation in the null case of no connectivity. For both rats, the BOLD signals are collected

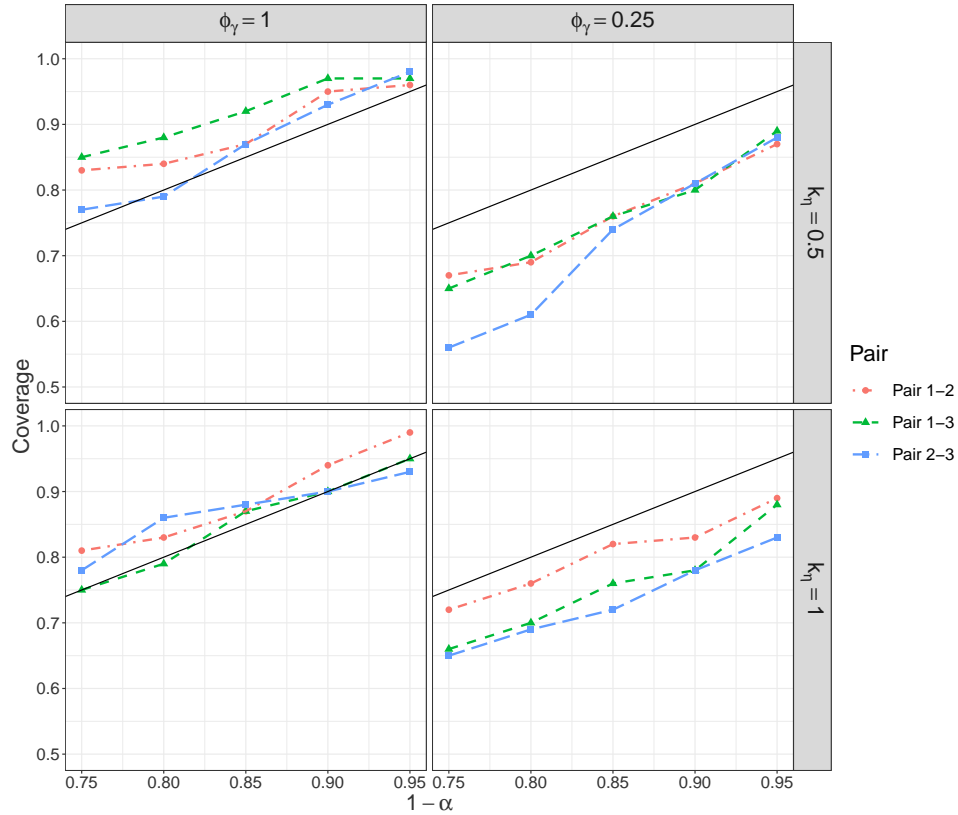


Fig 2: Coverage of confidence intervals. From top to bottom: weak signal, strong signal. From left to right: weak intra-regional correlation, strong intra-regional correlation. Black solid line denotes the desired $1 - \alpha$ coverage.

at the frequency of 2 Hz for the duration of 30 minutes. Preprocessing steps include motion removal and wavelet transformation of the original signals. As the wavelet transformation is linear, model (2.1) applies to the raw BOLD signals as well as the wavelet-transformed data, with the only difference being that t_m indexes different wavelet coefficients rather than time, although the time ordering is preserved. Wavelets provide a very adequate framework for analysing BOLD signals because of their flexibility and ability to deal with long-memory time series (Whitcher, Guttorp and Percival, 2000; Percival and Walden, 2006).

Popular wavelet methods such as the discrete wavelet transform (DWT) and maximal overlap discrete wavelet transform (MODWT) have been used for quantifying functional connectivity (Achard et al., 2006; Deuker et al., 2009; Vértes et al., 2012). For our analysis, we use DWT with Daubechies Least Asymmetric filter of length 8 as this transformation reduces the number of available wavelet coefficients. This makes DWT more computationally attractive for the method proposed in this paper. The wavelet coefficients of level 4 were chosen according to Becq et al. (2020) where systematic variables such as heart rat or body temperature were found to perturb the functional connectivity less relative to other choices. For more details on these preprocessing steps, we refer readers to Becq et al. (2020).

TABLE 2

Names of the 21 regions of the rat brain chosen for study, and their corresponding labels.

Region name	Region label
anterior cingulate cortex	ACC
amygdalopiriform transition area right	APir r
auditory cortex right	AU r
entorhinal area right	Ent r
parietal association cortex right	Par r
primary motor cortex right	M1 r
supplementary motor cortex right	M2 r
retrosplenial cortex right	RSC r
somatosensory 1 right, barrel field	S1BF r
amygdalopiriform transition area left	APir l
auditory cortex left	AU l
entorhinal area left	Ent l
parietal association cortex left	Par l
primary motor cortex left	M1 l
supplementary motor cortex left	M2 l
retrosplenial cortex left	RSC l
somatosensory 1 left, barrel field	S1BF l
hypothalamic region right	H r
hippocampus right	HIP r
hypothalamic region left	H l
hippocampus left	HIP l

We focus on 21 regions of interest out of 51 regions, defined by the custom atlas used in [Becq et al. \(2020\)](#). Full regions names and corresponding labels can be found in Table 2. These regions consist of 10 bi-lateral region pairs (one each in the left and right hemispheres), and one central region (ACC). For each pair of regions (j, j') , $1 \leq j < j' \leq 21$, we first obtain $\hat{\rho}_{jj'}^{\text{ReML}}$, then use the asymptotic distribution derived in Theorem 2.30 to calculate the z -scores of these estimators. In particular, we parameterized the inter and intra-regional covariance matrices with radial basis function (RBF), also known as Gaussian, kernels and the spatial correlation matrix with the Matérn-5/2 kernel. A cubic B-spline basis of size $K = 30$ was used in *Stage 1* of the estimation. As previously mentioned, we use the BOBYQA for real data application for its superior stability. Detailed steps of the optimization are outlined in Algorithms 1 and 2 in Appendix A, and were implemented in an R package that can be found on Github (<https://github.com/cbtran/qfuncMM>). We further adopt the Benjamini–Yekutieli (BY) procedure ([Benjamini and Yekutieli, 2001](#)) to perform hypothesis testing for significant correlations between pairs of regions. The BY procedure is used to control the false discovery rate (FDR) under arbitrary dependence assumptions ([Logan and Rowe, 2004](#)), which is suitable for this application. Furthermore, since discoveries are expected for the live rat, controlling FDR means that false discoveries are not penalized as harshly as the controlling the family-wise error rate, which is equivalent to FDR only under the global null in which all inter-regional correlations are zero, making FDR less conservative and more reasonable for this application.

As an initial check on the model, data from the dead rat were analyzed. The smallest unadjusted p -value was 0.157, so that no significant correlations were discovered even without the BY adjustment, using any conventional level of significance. In comparison with [Becq et al. \(2020\)](#), this results lines up with their group analysis of several dead rats, although their methodology did lead to a few spurious edges when applied to individual rats as done here.

Furthermore, in the case of a live rat, we compare the result with the network of the same rat in [Becq et al. \(2020\)](#). Here, significant edges were detected by applying the BY procedure with level $q = 0.01$. Figure 3a shows the estimated $\hat{\rho}^{\text{ReML}}$ for all 21 studied regions. Without

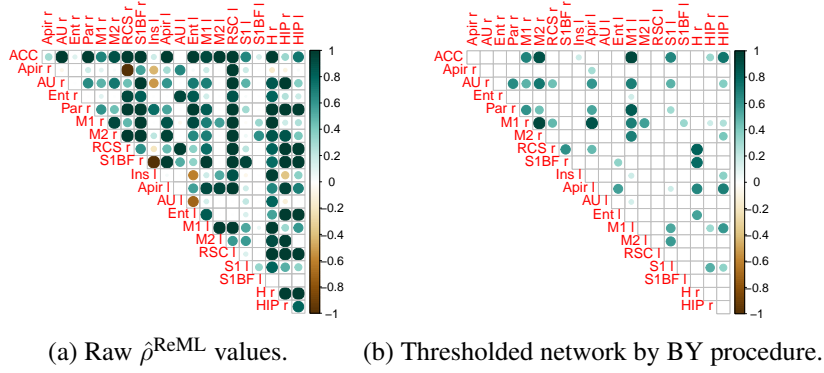


Fig 3: Brain network of anesthetized rat 20160616_145220, Eto-L.

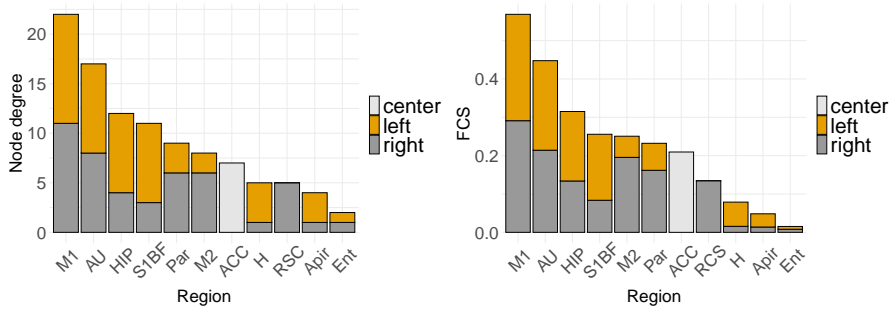


Fig 4: Node degree (a) and FCS (b) of anesthetized rat 20160616_145220, Eto-L.

quantifying their uncertainty, these raw estimates should not be used directly to represent a brain network since large values might also correspond to large variations. Therefore, the network is constructed by performing the BY procedure and is represented in Figure 3b by showing the estimates $\hat{\rho}^{\text{ReML}}$ for significant edges as the upper triangular portion of the weighted adjacency matrix.

To further summarize the role of each region in the network, we also constructed node degree (ND) and functional connectivity strength (FCS) plots in Figure 4. Here, ND is the total number of edges for each region, while FCS is the average correlation estimate across detected edges for the region. At rest, networks should be roughly symmetric, so Figure 4 stacks these quantities vertically for bilateral regions, which only excludes ACC. The minor degree of asymmetry in both ND and FCS metrics between left and right regions is similar to that observed in Becq et al. (2020). We found that our result is mostly consistent with the previous study. For example, under the same Etomidate anesthetic, regions such as ACC, M1, M2, AU were found there to be highly connected, and the proposed model also estimated a high connectivity level for these regions. On the other hand, for Ent and RSC, which are commonly found to be disconnected for several live rats under this anaesthetic (Becq et al., 2020), a low level of connectivity is also observed in our result. Overall, the network constructed using the proposed model was more sparse, having 30 fewer edges than the network constructed using $\hat{\rho}^{\text{CA}}$ after applying the same BY procedure. The ReML network discovered 22 edges that do not appear in the Correlation of Averages network, 17 of which belong to one of the regions ACC, M1, M2, and AU.

5. Discussion. A novel spatiotemporal model for voxel-level BOLD signals has been proposed that explicitly models the regional signals that drive both inter-regional and intra-regional correlation, local spatiotemporal fields that allow for idiosyncratic, heterogeneous intra-regional correlation, and measurement error. By fully addressing the spatiotemporal dependency structure, a coherent quantification of inter-regional brain connectivity emerges, together with a well-established and justified estimation approach. Large sample properties were established with mild conditions on the smoothness of covariance structure and the decaying rate of dependency. Simulation studies showed that the key inter-regional correlation parameters can be accurately estimated, with stark advantages compared conventional Pearson correlation of averages in the presence of strong spatiotemporal noise. Furthermore, the application on rat data showed that our findings are mostly consistent with previously established results, which indicates that our model can produce reasonable results while being superior in certain noisy regimes. In particular, where the network constructed by the proposed model differed from the established correlation of averages network is precisely those cases in which our simulation studies indicate the superior reliability of $\hat{\rho}^{\text{ReML}}$ compared to $\hat{\rho}^{\text{CA}}$. Further development of the method to make it applicable to a wider array of data sets includes computational tools for a more flexible collection of dependence structures. While this paper has focused on the Gaussian case, alternative estimators in non-Gaussian linear mixed models can readily be applied in the proposed two-stage approach.

Although designed for the purpose of estimating functional connectivity, the proposed model could be useful for quantifying dependence amongst spatially grouped time series in other contexts. In climate studies, for example, the data sets consist of time series measuring the temperature for a given area. Similar models, as proposed here, were used to predict the temperature on a large area (Hengl et al., 2012; Gräler, Pebesma and Heuvelink, 2016). Another example can be found in disease propagation, where the data sets consist of time series measuring the number of positive cases of COVID in a specific area (Bartolucci and Farcomeni, 2022). The model used is a Markov Chain where for each area the sequence of latent variables across time follows a Markov chain with initial and transition probabilities that also depend on latent variables in neighboring areas.

Lastly, the data illustrations have utilized a pre-specified set of regions for functional connectivity analysis (Biswal et al., 1995). This approach relies on a predefined brain parcellation, commonly in form of an atlas, to determine regions of interest. As a result, different subjects are also assumed to have the same functional network nodes. Recently, data-driven methods for functional connectivity analysis have been proposed (Van Den Heuvel and Pol, 2010; Lv et al., 2018), thus allowing nodes in functional networks to be subject-specific (Cui et al., 2020; Michon et al., 2022). It will be interesting to investigate if our proposed methods for quantifying functional connectivity can be combined with subject-specific region discovery in order to simultaneously study variability in the spatial distribution of functional connectivity nodes as well as connections between them.

Acknowledgments. The authors acknowledge the following computational facilities for providing computational resources and technical support that have contributed to the results reported within this publication:

1. The Office of Research Computing at Brigham Young University. URL: <https://rc.byu.edu>.
2. The Center for Scientific Computing (CSC), which administrated funds from the National Science Foundation (CNS-1725797) for the purchase of computational facilities. The CSC is supported by the California NanoSystems Institute and the Materials Research Science and Engineering Center (MRSEC; NSF DMR 1720256) at UC Santa Barbara. URL: <https://csc.cnsi.ucsb.edu>.

The authors also gratefully acknowledge the support of this research provided by grants from the US National Science Foundation’s Collaborative Research in Computational Neuroscience program (Award IIS-2135859) and the French National Research Agency.

APPENDIX A: SCALABLE INFERENCE APPROACHES

Common computation techniques, such as direction inversion or Cholesky decomposition of the covariance matrices, result in $O(N^3)$ time complexity, where $N = L_j \times M$ for a single, and $N = (L_j + L_{j'}) \times M$ for a region pair. Thus, we exploit the structures of the covariance matrices to improve scalability.

A.1. Stage 1: Region-specific Model. Recall that in region-specific model, the covariance matrix has the form $\mathbf{V}_j(\boldsymbol{\theta}_j) = \mathbf{C}_j \otimes \mathbf{B}_j + \sigma^2 \mathbf{I}$. As shown in Saatchi (2011), this Kronecker structure leads to an efficient algorithm for evaluating Gaussian (restricted) log-likelihood. In particular, let $\mathbf{C}_j = \mathbf{Q}_C \boldsymbol{\Lambda}_C \mathbf{Q}_C^\top$ and $\mathbf{B}_j = \mathbf{Q}_B \boldsymbol{\Lambda}_B \mathbf{Q}_B^\top$ be eigendecompositions of \mathbf{C}_j and \mathbf{B}_j , respectively. Then, for a vector $\mathbf{z} \in \mathbb{R}^N$, $N = L_j \times M$, we have

$$\begin{aligned} \mathbf{V}_j^{-1} \mathbf{z} &= (\mathbf{C}_j \otimes \mathbf{B}_j + \sigma^2 \mathbf{I})^{-1} \mathbf{z} \\ (A.1) \quad &= (\mathbf{Q}_C \otimes \mathbf{Q}_B) (\boldsymbol{\Lambda}_C \otimes \boldsymbol{\Lambda}_B + \sigma^2 \mathbf{I})^{-1} (\mathbf{Q}_C^\top \otimes \mathbf{Q}_B^\top) \mathbf{z}, \end{aligned}$$

where $(\boldsymbol{\Lambda}_C \otimes \boldsymbol{\Lambda}_B + \sigma^2 \mathbf{I})$ is a diagonal matrix, and $(\mathbf{Q}_C^\top \otimes \mathbf{Q}_B^\top) \mathbf{z}$ can be efficiently computed using

$$(\mathbf{Q}_C^\top \otimes \mathbf{Q}_B^\top) \mathbf{z} = \text{vectorize}(\mathbf{Q}_B^\top \mathbf{Z} \mathbf{Q}_C),$$

where $\mathbf{z} = \text{vectorize}(\mathbf{Z})$ for $\mathbf{Z} \in \mathbb{R}^{M \times L_j}$. In addition,

$$(A.2) \quad \log \det(\mathbf{V}_j) = \sum_{l=1}^{L_j} \sum_{m=1}^M [(\boldsymbol{\Lambda}_C)_l (\boldsymbol{\Lambda}_B)_m + \sigma^2].$$

Since the most computationally intensive step is computing eigendecompositions of \mathbf{C}_j and \mathbf{B}_j , time complexity of this inference approach is $O(L_j^3 + M^3)$ for ML and $O(L_j^3 + M^3 + K^3)$ for ReML where K is the B-spline degrees of freedom instead of $O(L_j^3 M^3)$ when using direct inversion or Cholesky decomposition. We then estimate region-specific parameters using Algorithm 1.

Algorithm 1 Region-specific model

Input: Data matrix \mathbf{X}_j , design matrix \mathbf{G}_j , initial values $\boldsymbol{\theta}_j^{(0)}$ and $\mathbf{v}_j^{(0)}$, number of iterations T

$\mathbf{r}_j^{(0)} \leftarrow \mathbf{X}_j - \mathbf{G}_j \mathbf{v}_j^{(0)}$

for $t \in 1 : T$ **do**

Compute $\mathbf{C}_j, \mathbf{B}_j$

Compute eigendecompositions $\mathbf{C}_j = \mathbf{Q}_C \boldsymbol{\Lambda}_C \mathbf{Q}_C^\top$ and $\mathbf{B}_j = \mathbf{Q}_B \boldsymbol{\Lambda}_B \mathbf{Q}_B^\top$

Evaluate (restricted) log-likelihood

if Convergence **then**

Break

else

Update $\boldsymbol{\theta}_j^{(t)}$ and $\mathbf{v}_j^{(t)}$

end if

end for

Output: $\hat{\boldsymbol{\theta}}_j$ and $\hat{\mathbf{v}}_j$

A.2. Stage 2: Inter-regional model. For inter-regional model, we use the Schur complement (Petersen and Pedersen, 2008) to efficiently evaluate the loss function. For simplicity, let

$$(A.3) \quad \mathbf{V}(\boldsymbol{\theta}) = \begin{bmatrix} \mathbf{V}_{11} & \mathbf{V}_{12} \\ \mathbf{V}_{12}^\top & \mathbf{V}_{22} \end{bmatrix},$$

$$(A.4) \quad \mathbf{W} = \mathbf{V}_{11} - \mathbf{V}_{12} \mathbf{V}_{22}^{-1} \mathbf{V}_{12}^\top.$$

Then we have

$$(A.5) \quad \log \det(\mathbf{V}) = \log \det(\mathbf{W}) + \log \det(\mathbf{V}_{22}).$$

For a vector $\mathbf{z} \in \mathbb{R}^N$, $N = (L_j + L_k) \times M$, we want to compute $\mathbf{V}^{-1} \mathbf{z}$, which is equivalent to solving linear systems

$$(A.6) \quad \begin{bmatrix} \mathbf{V}_{11} & \mathbf{V}_{12} \\ \mathbf{V}_{12}^\top & \mathbf{V}_{22} \end{bmatrix} \begin{bmatrix} \mathbf{z}_1 \\ \mathbf{z}_2 \end{bmatrix} = \begin{bmatrix} \mathbf{b}_1 \\ \mathbf{b}_2 \end{bmatrix},$$

where $\mathbf{z} = \begin{bmatrix} \mathbf{z}_1 \\ \mathbf{z}_2 \end{bmatrix}$. We first solve for \mathbf{b}_1 using

$$(A.7) \quad \mathbf{b}_1 = \mathbf{W}^{-1} (\mathbf{z}_1 - \mathbf{V}_{12} \mathbf{V}_{22}^{-1} \mathbf{z}_2).$$

Then we use \mathbf{b}_1 to solve for \mathbf{b}_2 in (A.6).

Note that these computations of log-determinant and matrix inversion can be further improved by Cholesky decomposition of block components. For example, let \mathbf{W}^{Chol} be the Cholesky decomposition of \mathbf{W} such as

$$(A.8) \quad \mathbf{W} = \mathbf{W}^{Chol} (\mathbf{W}^{Chol})^\top.$$

Then

$$(A.9) \quad \log \det(\mathbf{W}) = 2 \times \sum_{i=1}^{L_j \times M} \log(\mathbf{W}_{ii}^{Chol}),$$

and for a vector $\mathbf{z} \in \mathbb{R}^{L_j \times M}$, $\mathbf{W}^{-1} \mathbf{z}$ can be computed using forward-backward substitution. Finally, inter-regional parameters are estimated using Algorithm 2.

Algorithm 2 Inter-regional model

Input: Data matrix $\mathbf{X} = [\mathbf{X}_j^\top \mathbf{X}_k^\top]^\top$, design matrix \mathbf{Z} , region-specific estimates $\mathbf{C}_j, \mathbf{B}_j, \mathbf{C}_k, \mathbf{B}_k$, initial values $\boldsymbol{\theta}^{(0)}$ and $\boldsymbol{\mu}^{(0)}$, number of iteration T

$\mathbf{r}^{(0)} \leftarrow \mathbf{X} - \mathbf{Z} \boldsymbol{\mu}^{(0)}$

for $t \in 1 : T$ **do**

 Compute \mathbf{A}

 Compute \mathbf{V}_{22} and \mathbf{W}

 Evaluate (restricted) log-likelihood

if Convergence **then**

 Break

else

 Update $\boldsymbol{\theta}^{(t)}$ and $\boldsymbol{\mu}^{(t)}$

end if

end for

Output: $\hat{\boldsymbol{\theta}}$ and $\hat{\boldsymbol{\mu}}$

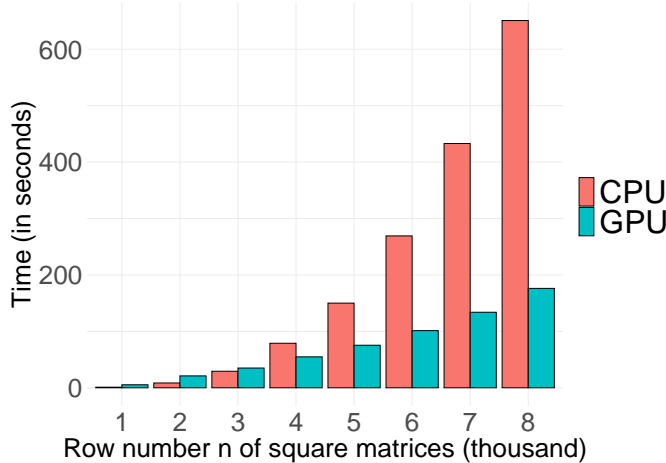


Fig 5: Comparison between time complexity of matrix operations, inversion and log determinant, using CPU and GPU.

A.3. Hardware acceleration. Despite our two-stage approach effectively reducing the dimension of parameter space, likelihood evaluation remains expensive due to the large dimensionality of our covariance matrix. To speed up the computation, we utilize parallel computing to run estimations simultaneously. Since it is well-known that Graphics Processing Units (GPU) may provide a significant speed-up when compared with Central Processing Unit (CPU) for large-scale computations (Krizhevsky, Sutskever and Hinton, 2012; Gardner et al., 2018), we delegate level 3 Basic Linear Algebra Subprograms (BLAS) matrix operations to GPU using NVIDIA’s CUDA framework to accelerate matrix calculations. These operations are sufficiently complex (e.g., matrix-matrix product, solving triangular matrix equations) to ensure the speed gain of using GPU outshines the overhead of transferring data between CPU and GPU. To demonstrate this point, we benchmarked matrix inversion and log determinant calculations, which are commonly encountered in log likelihood evaluation, using CPU and GPU for $n \times n$ matrices, $n = 1000, 2000, \dots, 8000$. Figure 5 shows a decisive advantage of GPU calculation when matrix size grows over a certain level (4000×4000 in our experiment). In our data application, the covariance matrix could easily go beyond 10000 rows (columns) so using GPU acceleration could greatly improve computation efficiency.

APPENDIX B: ADDITIONAL SIMULATION RESULTS

This section reports additional results under the simulation design discussed in Section 3. While the results reported in the text correspond to weak ($k_\eta = 0.5$) and strong ($k_\eta = 1$) signal strengths, those reported in Table 3 and Figure 6 below present results for the case of a very strong signal ($k_\eta = 1.5$).

TABLE 3

Estimate of correlation coefficients from simulated data. Two levels of intra-regional correlation, $\phi_\gamma = 0.25$ (strong) and $\phi_\gamma = 1$ (weak), and three levels of inter-regional correlation, $\rho = 0.1, 0.35, 0.6$ are used along with a very strong signal $k_\eta = 1.5$. The three estimators are Pearson correlation of average (CA), Pearson correlation of fixed-effect estimate (FE), and the proposed ReML estimator (ReML).

Signal	Intra-correlation	ρ_{True}	Type	RMSE	Bias	SD
$k_\eta = 1.5$	$\phi_\gamma = 1$	0.1	ReML	0.1550	0.0189	0.1547
			FE	0.2949	0.0570	0.2908
			CA	0.2837	0.0484	0.2809
		0.35	ReML	0.1521	0.0014	0.1529
			FE	0.2724	0.0444	0.2701
			CA	0.2613	0.0454	0.2586
	0.6	ReML	0.1104	0.0196	0.1092	
		FE	0.2404	0.0726	0.2303	
		CA	0.2315	0.0788	0.2188	
	$\phi_\gamma = 0.25$	0.1	ReML	0.1961	0.0256	0.1954
			FE	0.2961	0.0242	0.2966
			CA	0.2657	0.0068	0.2669
0.35		ReML	0.1843	0.0230	0.1838	
		FE	0.2965	0.1301	0.2678	
		CA	0.3243	0.1720	0.2763	
0.6	ReML	0.1456	0.0027	0.1463		
	FE	0.3144	0.1959	0.2472		
	CA	0.3591	0.2594	0.2496		

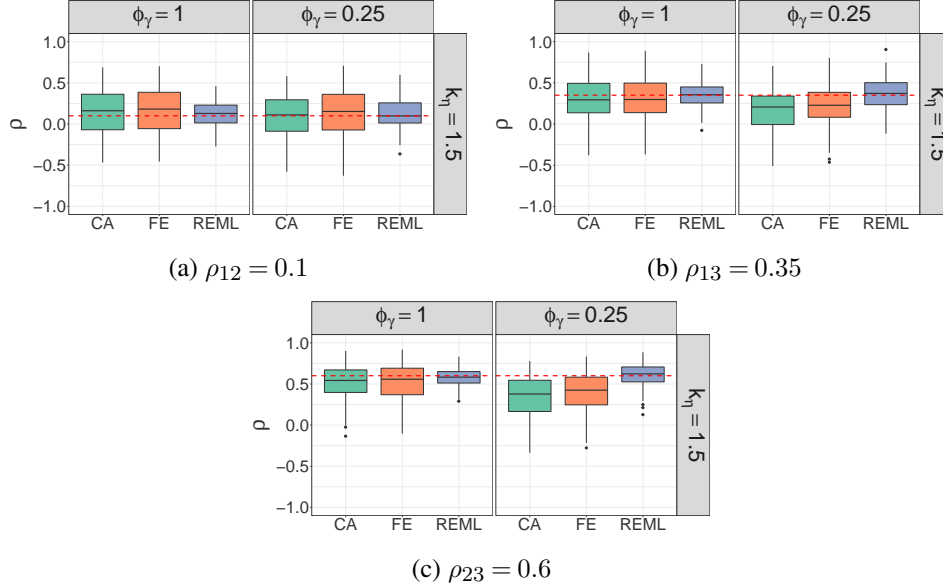


Fig 6: Empirical distribution of estimated inter-regional correlations with very strong signal $k_\eta = 1.5$: (a) Weak inter-regional correlation, (b) Medium inter-regional correlation, (c) Strong inter-regional correlation. In each subfigure: two intra-regional correlation rates are $\phi_\gamma = 0.25$ (strong) and $\phi_\gamma = 1$ (weak); three estimators are Pearson correlation of average (CA), Pearson correlation of fixed-effect estimate (FE), ReML estimator (ReML). Dashed line denotes the true value of inter-regional correlation.

REFERENCES

- ACHARD, S. and GANNAZ, I. (2019). Wavelet-based and Fourier-based multivariate Whittle estimation: multi-wave. *Journal of Statistical Software* **89** 1–31.
- ACHARD, S., SALVADOR, R., WHITCHER, B., SUCKLING, J. and BULLMORE, E. (2006). A resilient, low-frequency, small-world human brain functional network with highly connected association cortical hubs. *Journal of Neuroscience* **26** 63–72.
- ACHARD, S., COEURJOLLY, J.-F., MARCILLAUD, R. and RICHIARDI, J. (2011). fMRI functional connectivity estimators robust to region size bias. In *2011 IEEE Statistical Signal Processing Workshop (SSP)* 813–816. IEEE.
- AFYOUNI, S., SMITH, S. M. and NICHOLS, T. E. (2019). Effective degrees of freedom of the Pearson’s correlation coefficient under autocorrelation. *NeuroImage* **199** 609–625. <https://doi.org/10.1016/j.neuroimage.2019.05.011>
- AZEVEDO, T., CAMPBELL, A., ROMERO-GARCIA, R., PASSAMONTI, L., BETHLEHEM, R. A., LIÒ, P. and TOSCHI, N. (2022). A deep graph neural network architecture for modelling spatio-temporal dynamics in resting-state functional MRI data. *Medical Image Analysis* **79** 102471. <https://doi.org/10.1016/j.media.2022.102471>
- BARTOLUCCI, F. and FARCOMENI, A. (2022). A spatio-temporal model based on discrete latent variables for the analysis of COVID-19 incidence. *Spatial Statistics* **49** 100504.
- BEQG, G., HABET, T., COLLOMB, N., FAUCHER, M., DELON-MARTIN, C., COIZET, V., ACHARD, S. and BARBIER, E. L. (2020). Functional connectivity is preserved but reorganized across several anesthetic regimes. *NeuroImage* **219** 116945.
- BENJAMINI, Y. and YEKUTIELI, D. (2001). The Control of the False Discovery Rate in Multiple Testing under Dependency. *The Annals of Statistics* **29** 1165–1188.
- BISWAL, B., ZERRIN YETKIN, F., HAUGHTON, V. M. and HYDE, J. S. (1995). Functional connectivity in the motor cortex of resting human brain using echo-planar MRI. *Magnetic Resonance in Medicine* **34** 537–541. <https://doi.org/10.1002/mrm.1910340409>
- BOWMAN, F. D. (2007). Spatiotemporal models for region of interest analyses of functional neuroimaging data. *Journal of the American Statistical Association* **102** 442–453.
- CHAIMOW, D., YACOB, E., UĞURBİL, K. and SHMUEL, A. (2018). Spatial specificity of the functional MRI blood oxygenation response relative to neuronal activity. *NeuroImage* **164** 32–47.
- CRESSIE, N. and LAHIRI, S. N. (1993). The asymptotic distribution of REML estimators. *Journal of Multivariate Analysis* **45** 217–233.
- CRESSIE, N. and LAHIRI, S. N. (1996). Asymptotics for REML estimation of spatial covariance parameters. *Journal of Statistical Planning and Inference* **50** 327–341.
- CUI, Z., LI, H., XIA, C. H., LARSEN, B., ADEBIMPE, A., BAUM, G. L., CIESLAK, M., GUR, R. E., GUR, R. C., MOORE, T. M., OATHES, D. J., ALEXANDER-BLOCH, A. F., RAZNAHAN, A., ROALF, D. R., SHINOHARA, R. T., WOLF, D. H., DAVATZIKOS, C., BASSETT, D. S., FAIR, D. A., FAN, Y. and SATTERTHWAITE, T. D. (2020). Individual Variation in Functional Topography of Association Networks in Youth. *Neuron* **106** 340–353.e8. <https://doi.org/10.1016/j.neuron.2020.01.029>
- DELICADO, P., GIRALDO, R., COMAS, C. and MATEU, J. (2010). Statistics for spatial functional data: some recent contributions. *Environmetrics: The Official Journal of The International Environmetrics Society* **21** 224–239.
- DEUKER, L., BULLMORE, E. T., SMITH, M., CHRISTENSEN, S., NATHAN, P. J., ROCKSTROH, B. and BASSETT, D. S. (2009). Reproducibility of graph metrics of human brain functional networks. *Neuroimage* **47** 1460–1468.
- EICKHOFF, S. B., YEO, B. and GENON, S. (2018). Imaging-based parcellations of the human brain. *Nature Reviews Neuroscience* **19** 672–686.
- FRENCH, J. P. and KOKOSZKA, P. S. (2021). A sandwich smoother for spatio-temporal functional data. *Spatial Statistics* **42** 100413.
- GARDNER, J., PLEISS, G., WEINBERGER, K. Q., BINDEL, D. and WILSON, A. G. (2018). GPyTorch: Black-box Matrix-Matrix Gaussian Process Inference with GPU Acceleration. In *Advances in Neural Information Processing Systems* (S. BENGIO, H. WALLACH, H. LAROCHELLE, K. GRAUMAN, N. CESA-BIANCHI and R. GARNETT, eds.) **31**. Curran Associates, Inc.
- GRÄLER, B., PEBESMA, E. J. and HEUVELINK, G. B. (2016). Spatio-temporal interpolation using gstat. *The R Journal* **8** 204.
- GROMENKO, O., KOKOSZKA, P., ZHU, L. and SOJKA, J. (2012). Estimation and testing for spatially indexed curves with application to ionospheric and magnetic field trends. *The Annals of Applied Statistics* **6** 669–696.
- HARVILLE, D. A. (1974). Bayesian inference for variance components using only error contrasts. *Biometrika* **61** 383–385.

- HENGL, T., HEUVELINK, G., PERČEC TADIĆ, M. and PEBESMA, E. J. (2012). Spatio-temporal prediction of daily temperatures using time-series of MODIS LST images. *Theoretical and Applied Climatology* **107** 265–277.
- HÖRMANN, S. and KOKOSZKA, P. (2011). Consistency of the mean and the principal components of spatially distributed functional data. In *Recent Advances in Functional Data Analysis and Related Topics* 169–175. Springer.
- JENNRICH, R. I. and SCHLUCHTER, M. D. (1986). Unbalanced repeated-measures models with structured covariance matrices. *Biometrics* **42** 805–820. <https://doi.org/10.2307/2530695>
- KAISER, M. (2011). A tutorial in connectome analysis: topological and spatial features of brain networks. *NeuroImage* **57** 892–907. <https://doi.org/10.1016/j.neuroimage.2011.05.025>
- KRIZHEVSKY, A., SUTSKEVER, I. and HINTON, G. E. (2012). ImageNet Classification with Deep Convolutional Neural Networks. In *Advances in Neural Information Processing Systems* (F. PEREIRA, C. J. BURGESS, L. BOTTOU and K. Q. WEINBERGER, eds.) **25**. Curran Associates, Inc.
- LINDSTROM, M. J. and BATES, D. M. (1988). Newton-Raphson and EM algorithms for linear mixed-effects models for repeated-measures data. *Journal of the American Statistical Association* **83** 1014–1022.
- LOGAN, B. R. and ROWE, D. B. (2004). An evaluation of thresholding techniques in fMRI analysis. *NeuroImage* **22** 95–108. <https://doi.org/10.1016/j.neuroimage.2003.12.047>
- LOHMANN, G., STELZER, J., LACOSSE, E., KUMAR, V. J., MUELLER, K., KUEHN, E., GRODD, W. and SCHEFFLER, K. (2018). LISA improves statistical analysis for fMRI. *Nature Communications* **9** 1–9.
- LV, H., WANG, Z., TONG, E., WILLIAMS, L. M., ZAHARCHUK, G., ZEINEH, M., GOLDSTEIN-PIEKARSKI, A. N., BALL, T. M., LIAO, C. and WINTERMARK, M. (2018). Resting-state functional MRI: everything that nonexperts have always wanted to know. *American Journal of Neuroradiology* **39** 1390–1399. <https://doi.org/10.3174/ajnr.A5527>
- MCINTOSH, A. R., CHAU, W. and PROTZNER, A. B. (2004). Spatiotemporal analysis of event-related fMRI data using partial least squares. *NeuroImage* **23** 764–775. <https://doi.org/10.1016/j.neuroimage.2004.05.018>
- MESKALDJI, D. E., OTTET, M.-C., CAMMOUN, L., HAGMANN, P., MEULI, R., ELIEZ, S., THIRAN, J. P. and MORGENTHALER, S. (2011). Adaptive strategy for the statistical analysis of connectomes. *PloS One* **6** e23009. <https://doi.org/10.1371/journal.pone.0023009>
- MICHON, K. J., KHAMMASH, D., SIMMONITE, M., HAMLIN, A. M. and POLK, T. A. (2022). Person-specific and precision neuroimaging: Current methods and future directions. *NeuroImage* **263** 119589. <https://doi.org/10.1016/j.neuroimage.2022.119589>
- MOGHIMI, P., DANG, A. T., DO, Q., NETOFF, T. I., LIM, K. O. and ATLURI, G. (2022). Evaluation of functional MRI-based human brain parcellation: a review. *Journal of Neurophysiology* **128** 197–217. PMID: 35675446. <https://doi.org/10.1152/jn.00411.2021>
- NOCEDAL, J. (1980). Updating quasi-Newton matrices with limited storage. *Mathematics of Computation* **35** 773–782. <https://doi.org/10.1090/S0025-5718-1980-0572855-7>
- PARK, J. Y. and FIECAS, M. (2022). CLEAN: Leveraging spatial autocorrelation in neuroimaging data in clusterwise inference. *NeuroImage* **255** 119192.
- PERCIVAL, D. B. and WALDEN, A. T. (2006). *Wavelet Methods for Time Series Analysis* **4**. Cambridge University Press.
- PETERSEN, K. B. and PEDERSEN, M. S. (2008). The Matrix Cookbook. *Technical University of Denmark* **7** 510.
- PETERSEN, A., ZHAO, J., CARMICHAEL, O. and MÜLLER, H.-G. (2016). Quantifying individual brain connectivity with functional principal component analysis for networks. *Brain Connectivity* **6** 540–547.
- PINHEIRO, J. and BATES, D. (2006). *Mixed-effects models in S and S-PLUS*. Springer Science & Business Media.
- POWELL, M. J. (2009). The BOBYQA algorithm for bound constrained optimization without derivatives. *Cambridge NA Report NA2009/06*, University of Cambridge, Cambridge **26**.
- RICHIARDI, J., ACHARD, S., BUNKE, H. and VAN DE VILLE, D. (2013). Machine learning with brain graphs: predictive modeling approaches for functional imaging in systems neuroscience. *IEEE Signal Processing Magazine* **30** 58–70.
- SAATCHI, Y. (2011). Scalable inference for structured Gaussian process models, PhD thesis, University of Cambridge.
- STEIN, M. L. (1999). *Interpolation of Spatial Data: Some Theory for Kriging*. Springer Science & Business Media.
- TAYLOR, J. E. and WORSLEY, K. J. (2007). Detecting sparse signals in random fields, with an application to brain mapping. *Journal of the American Statistical Association* **102** 913–928.
- TERMENON, M., JAILLARD, A., DELON-MARTIN, C. and ACHARD, S. (2016). Reliability of graph analysis of resting state fMRI using test-retest dataset from the Human Connectome Project. *NeuroImage* **142** 172–187.

- VAN DEN HEUVEL, M. P. and POL, H. E. H. (2010). Exploring the brain network: a review on resting-state fMRI functional connectivity. *European Neuropsychopharmacology* **20** 519–534.
- VÉRTES, P. E., ALEXANDER-BLOCH, A. F., GOGTAY, N., GIEDD, J. N., RAPOPORT, J. L. and BULLMORE, E. T. (2012). Simple models of human brain functional networks. *Proceedings of the National Academy of Sciences* **109** 5868–5873.
- WHITCHER, B., GUTTORP, P. and PERCIVAL, D. B. (2000). Wavelet analysis of covariance with application to atmospheric time series. *Journal of Geophysical Research* **105(D11)** 941-962.
- WOOLRICH, M. W., JENKINSON, M., BRADY, J. M. and SMITH, S. M. (2004). Fully Bayesian spatio-temporal modeling of fMRI data. *IEEE Transactions on Medical Imaging* **23** 213–231.
- YARGER, D., STOEV, S. and HSING, T. (2022). A functional-data approach to the Argo data. *The Annals of Applied Statistics* **16** 216–246.
- ZALESKY, A., FORNITO, A. and BULLMORE, E. (2012). On the use of correlation as a measure of network connectivity. *NeuroImage* **60** 2096–2106.
- ZHANG, H. and LI, Y. (2022). Unified principal component analysis for sparse and dense functional data under spatial dependency. *Journal of Business & Economic Statistics* **40** 1523-1537. <https://doi.org/10.1080/07350015.2021.1938085>
- ZHANG, L., GUINDANI, M., VERSACE, F. and VANNUCCI, M. (2014). A spatio-temporal nonparametric Bayesian variable selection model of fMRI data for clustering correlated time courses. *NeuroImage* **95** 162–175.